Supporting Information

Kaushal et al. 10.1073/pnas.1401657111

SI Results and Discussion

Small Subunit Body. Similar to that of S8 in bacterial ribosome, the density assigned to mito-specific mitochondrial ribosomal protein (MRP) S28 occupies the central position on the solvent side of the mito-small subunit (SSU) body. It interacts with the 12S rRNA helix 25 (h25) and a loop joining h20 and h22 (Fig. 2*B*) and with MRP S26, which in turn interacts with h7. The density assigned to mito-specific MRP S27, which is an α-helical protein, interacts mainly with the lower part of h44 and partially replaces the deleted segments of bacterial h44 and h11 in the mito-SSU (Fig. S2). Our docking did not account for the N-terminal domain (NTD) of MRP S27 (Fig. S5); however, an unoccupied cryo-EM density immediately next to the MRP S27 density would tightly accommodate the NTD (Fig. 1*C*). The density assigned to mito-specific MRP S30 is located just below h6 and h15, so that it would replace major portions of bacterial helices h6–h10 and h17, which are shorter or are completely absent in the mito-SSU (Fig. S2 *A* and *C*). The density assigned to MRP S31 occupies the lowest part of the mito-SSU and interacts only with two other mito-specific MRPs, S27 and S30 (Fig. 1 *C* and *D*).

SSU Head. A complex mass of density, situated at the top of h41 and MRPs S7 and S9, consistently segments into three distinct masses that tightly accommodate models for mito-specific MRPs S25, S34, and S35 (Fig. 1 *C* and *D*), suggesting that the most likely locations of both S25 and S34 are on the interface side of the mito-SSU, so that the density assigned to MRP S35 is partially sandwiched between MRPs S34 and S25 and is more exposed on the solvent side of the SSU. Both MRPs S25 and S35 also would interact with the apical region of h41.

The density previously identified as the beak lobe (1) is tentatively assigned to mito-specific MRP S23 (Fig. 1 *A* and *C*). This density partially replaces a small stretch of deleted bacterial rRNA, helix h33, and interacts with densities tentatively assigned to two other mito-specific MRPs, MRP S39 on the solvent side and MRP S22 on the interface side. In addition, MRP S39 also would interact with the mito-specific MRP S33 on the solvent side (Figs. 1*D* and 5*A*). The density assigned to MRP S33 is located just above MRP S2 and interacts with the conserved region of MRP S2 and h38, which is smaller in mito-SSU, and with a density that could be assigned to MRP S36 (Fig. 1*D*).

SI Materials and Methods

Isolation and Purification of the Mitoribosome. Mitochondria were isolated by homogenization of the *Bos taurus* liver followed by differential centrifugation in buffer containing 4 mM Hepes-KOH (pH 7.6), 440 mM mannitol, 2 mM EDTA, and 140 mM sucrose. Mitochondrial pellets were homogenized in buffer containing 0.26 M sucrose, 40 mM KCl, 15 mM $MgCl_2$, 15 mM Tris·HCl (pH 7.6), 6 mM β-mercaptoethanol, 0.8 mM EDTA, 0.05 mM spermine, and 0.05 mM spermidine and were centrifuged at 15, 000 rmp in a Sorvall SS34 rotor for 45 min. The concentration of KCl in the supernatant was increased to 300 mM, and the sample was layered on a 34% sucrose cushion and centrifuged at 35,000 rpm for 17 h in a Beckman Type Ti 70 rotor. Pellets were dissolved in buffer containing 20 mM Hepes-KOH (pH 7.6), 100 mM KCl, 20 mM $MgCl_2$, and 2 mM DTT and were subjected to 10–30% sucrose gradient centrifugation at 22,000 rpm using a Beckman SW32 rotor for 16 h. The 55S mitoribosome fractions were collected after fractionating the sucrose gradient in Teledyne ISCO gradient analyzer. The pooled fractions were pelleted by ultracentrifugation at 42,000 rpm for 6 h in a Beckman type Ti70 rotor. The 55S ribosomes were stored at −80 °C in storage buffer containing 20 mM Hepes-KOH (pH 7.6), 20 mM $MgCl_2$, 40 mM KCl, 20 mM DTT, and 5% glycerol. The 28S and 39S subunits were isolated by dialyzing the 55S preparation using storage buffer but with 1 mM $MgCl_2$ and then subjecting the dialyzed sample to 10–30% sucrose gradient centrifugation under the same buffer conditions at 22,000 rpm using a Beckman SW32 rotor for 16 h. Pooled fractions of 28S and 39S subunits, pelleted by ultracentrifugation at 42,000 rpm for 6 h in a Beckman type Ti70 rotor, were suspended in storage buffer and were stored in small aliquots at −80 °C.

Modeling of the 12S rRNA. ***Homology modeling.*** Because of the significant deletion of bacterial rRNA segments, several new loop regions are created in the mito-12S rRNA (2). Homology modeling of the homologous double-stranded rRNA segments of the 12S rRNA was relatively straightforward and was achieved using the 16S rRNA structure as a template (3), as described previously (4). In general, two rRNA helices connected by a bulge will have parallel axes (linear conformation) if the two strands of the bulge have a similar number of residues. For example, a 5–4 bulge connecting two helices displays a linear conformation, as seen in *Thermus thermophilus* 16S rRNA [e.g., 170–174 and 148–151 of Protein Data Bank (PDB) ID 1J5E] (3). In contrast, helices connected by a bulge with a large difference (>2) in the number of residues in each of the two loops often display a curved conformation (e.g., 700–705 and 685–687 of PDB ID 1J5E). Here we describe our approach of homologous loop modeling using a mito-rRNA segment as an example. A comparison of the *Bos taurus* 12S rRNA secondary structure (2) in helix 23 at positions 323–357 with that of the homologous region in *T. thermophilus* 16S rRNA (3) shows that the bulges have different number of residues (a 5–4 bulge and a 6–3 bulge, respectively). Because the sequences of the two bulges are significantly different, it was not clear whether we should use a linear 5–4 motif (which corresponds to the same region in the template *T. thermophilus* structure) or a curved 6–3 motif (which corresponds to the same number of residues in the two loops of the bulge) for modeling our target structure. First, we determined if a 5–4 bulge could be threaded onto a curved 6–3 motif. That is, could we replace the six-residue loop by a five-residue loop and the three-residue loop by a four-residue loop without disturbing structures of the two helices flanking the bulge? Close inspection of the structure of the curved 6–4 motif (residues 700–705 and 685–687 of PDB ID 1J5E) shows a stretched three-residue loop that can be replaced easily by a four-residue loop. Residues 701 and 702 in the six-residue loop are involved in a tight U-turn that can be replaced by a single residue to make a five-residue loop. From a structural point of view, both a linear motif and a curved motif can be accommodated. However, when the structure is docked into the cryo-EM map, the linear motif causes the entire hairpin loop (residues 334–345) to protrude from the cryo-EM map. Therefore, we selected the curved motif, which best explains the cryo-EM density.
Knowledge-based RNA loop modeling. To model larger RNA loops, we searched known RNA structures in PDB for candidate loops that fit the connecting criteria of the target molecule and match the cryo-EM density. This procedure is different from the RNA homology modeling described above, in which a well-defined secondary structure motif is available, and similarity in sequence is thought to imply similarity in structure. Here, when a loop connects known structural domains, the constraints derived from the surrounding residues and the cryo-EM density greatly reduce

the allowed flexibility for the loop. Thus, a known loop structure that satisfies the connection criteria, displays reasonable RNA stereochemistry in terms of bonds, angles, and dihedrals, and explains the features of the cryo-EM density is considered a good candidate that can be used to model the structure of the target loop. We selected loops whose ends overlap the ends of the loop that bridge across domains in the target RNA structures and simultaneously display satisfactory stereochemistry with respect to the surrounding steric environment. In particular, the ribose sugars at the loop ends were aligned with those of the target RNA. A small rmsd (<0.5 Å), in terms of both distance and orientation, was required between the end sugars from the loop and its target RNA. The candidate loops then were threaded with the target sequences. To investigate the interaction between the loop and its surroundings, van der Waals energies (E_{vdw}) were calculated using the standard Lennard–Jones 6–12 potential and the parameters of the AMBER force field (5). Small E_{vdw} ($<10^2$ kcal/mol) indicate the absence of poor (i.e., close) van der Waals contacts. The candidate loop structure that satisfies the end constraints (i.e., a small rmsd) with the minimum E_{vdw} was selected as the loop structure for the target molecule. We modeled the 277–283, 504–512, 532–536, 556–560, 590–602, 638–646, 690–695 and 733–743 loop regions using this approach.

Modeling of larger RNA bubble regions. Here we also describe our approach using a segment of the 12S rRNA as an example. According to the predicted secondary structure (2), a bubble region is located at residues 303–313, 384–388 in the 12S rRNA. These regions are nonhomologous in both sequence and secondary structure and are present between the rRNA helices 20 and 23. Because the region as a whole is relatively small (approximately seven base pairs with an internal loop constrained at both ends), the sequence was subjected to RNA secondary structural prediction using the MFOLD package as the starting point for construction of the model for this region (6). Seven canonical base pairs were identified. After considering all possible base pair types, we used two canonical base pairs (Fig. S2*A*) within this bubble region. A combined Monte Carlo docking and loop modeling algorithm (7) was used to model the structure of the bubble region in the presence of the surrounding residues, using criteria similar to those described above. Specifically, constraints were applied for the loop to connect the neighboring known structural domains and for the cryo-EM density, which together greatly reduce the flexibility allowed for the loop. Thus, a loop structure that satisfies the connection criteria, displays reasonable RNA stereochemistry in terms of bonds, angles, and dihedrals, and explains the features of the cryo-EM density was considered a good candidate. Finally, the candidates also needed to display satisfactory stereochemistry with respect to the surrounding steric environment, according to van der Waals energies.

Modeling of MRPs. MRPs were modeled into the cryo-EM density in multiple steps as depicted in the flow diagram (Fig. S3). Homology models for all MRPs were obtained using iterative threading assembly refinement (I-TASSER) server (8). We obtained five I-TASSER–based homology models for each MRP. The quality of each model was assessed by confidence score (C-score), and primarily models with high C-scores were selected.

For homologous MRPs the structure of the conserved domain was very similar in all five models. The conserved domain of the structure with highest C-score was docked first as a rigid body into the corresponding cryo-EM density, using Situs (9) and Chimera (10). Previously solved high-resolution structures of the bacterial ribosome (e.g., ref. 3) aided the molecular interpretation of the homologous portions of the MRPs. For most homologous MRPs the contact regions on the rRNA were preserved, allowing them to be docked into the ribosomal subunit in a similar manner to their bacterial counterparts, with only small adjustments required to match the features of the cryo-EM density. However, the placement of some of the MRPs, e.g., MRP S17, was guided primarily by the cryo-EM density because the deletion in some interacting rRNA helices had altered its orientation slightly (Fig. S6).

Most of homologous MRPs carry N-terminal and/or C-terminal extensions (NTEs and CTEs, respectively) of varying lengths (MRP S7 also carries an insertion) (Table S1). The mito-specific extensions were modeled by a three-step procedure. First, the contiguous cryo-EM density in the immediate vicinity of the N or C terminus that could accommodate the extension(s) of that MRP was identified. Second, all five structures of extension predicted by I-TASSER homology modeling were docked as a rigid body using Chimera (10), and The extension structure that best matched the features of the cryo-EM density and gave highest cross-correlation (CC) value was selected. Third, the conserved domain and modeled extension(s) were joined using Coot (11). In some cases, when loops were not fully accommodated into the cryo-EM density, they were modeled using model/refine loop program in Chimera (10). Homologous MRP models along with 12S rRNA were subjected to molecular dynamics flexible fitting (MDFF) (12) in vacuo for 100 ps while the geometrical restraints were imposed. The final model was validated using MolProbity (13).

Segmentation and Placement of Mito-Specific MRPs. The ensemble mass of the remaining cryo-EM density, i.e., the density left after modeling the 12S rRNA and homologous MRPs and their extensions/insertions, was subjected to Segger-based segmentation (14 and Fig. S4). Segger is a 3D density segmentation tool that uses the watershed method to find local minima within a given density gradient magnitude. The placement of 16 mito-specific MRPs also took into account the information available from chemical cross-linking (15) and immuno-EM (16) experiments and docking of homology models. For the Segger-based segmentation, the threshold of the cryo-EM map was adjusted so that characteristic structural features of the mito-SSU, such as the mRNA gate, beak lobe, and spur regions, maintain contact with rest of the SSU. However, possible noise (i.e., fragmented densities having fewer than 50 voxels) was excluded from this analysis. Many rounds of segmentation were performed by changing one parameter at a time, e.g., by using smoothing steps 8, 7, 6, and 5, and by varying the targeted number of segments to 20, 30, 40, and 50, respectively. (Results for 20 and 50 targeted segments are shown in Fig. S4.) A step size of one was maintained through all segmentations. The 20 largest segments obtained by using the smoothing step of 7 and 20 targeted segments were used in subsequent analysis. Of these, two segments that were too large to accommodate the largest of the 16 mito-specific MRPs were further ungrouped. This step gave us a total of 24 segments. The 16 most consistent regions that could accommodate MRPs within the molecular mass range of 11.5–77.7 kDa were selected (Table S2 and Fig. S4). The largest of the 16 segments was located in the mito-SSU head and was assigned to mito-specific MRP S39 (molecular mass, 77.7 kDa). The placement of MRP S39, along with MRP S36, also was supported by the cross-linking data with mitochondrial initiation factor 3 (15), suggesting that both these MRPs are situated close to the interface between the SSU-body and SSU-head domains. The remaining eight segments that were present mostly at the peripheral regions and that could not account for smallest (11.5 kDa) of the mito-specific MRPs were not used in subsequent analyses. These eight segments could belong either to unmodeled stretches of MRPs (Table S2) or to local conformational heterogeneity. For example, a segment found at the top of the SSU head, near MRPs S10 and S14, could correspond to unmodeled regions of neighboring MRPs.

To test the validity of this method further, an independent Segger-based segmentation of the cryo-EM mass for all MRPs, including the densities assigned to homologous MRPs, was performed (Fig. S4 *C* and *F*). When segmented for 31 regions,

segmented masses corresponding to 12 of 15 homologous MRPs match with their known positions closely, giving us further assurance regarding the segmentation obtained for the mito-specific MRPs. Three homologous MRPs that did not segment cleanly included densities for S18, which segmented as part of S11, the C-terminal helical segment of S21, which segmented as part of the density assigned to mito-specific MRP S36, and S24, which segmented as part of S10. A higher number of segmentations was not applied to split the fused densities for these homologous MRPs further.

A correlation between the molecular mass of MRP and the volume and surface area of segmented mito-specific MRP density was established, and each MRP was tentatively assigned to a particular cryo-EM mass. All five I-TASSER homology models for each mito-specific MRP possess similar structure in the core region; in most cases, however, terminal regions and some of the loop regions adopt slightly different conformations. Therefore, we focused primarily on the shape of the core structures that were consistent both in homology models and in the multiple segmentations of the cryo-EM density when displayed at higher-density threshold values. Each model of a MRP was docked into the tentatively assigned cryo-EM density using Situs (9), and the best model was selected based on CC values. The undocked regions of MRP (mostly terminal regions) were deleted from selected model (Table S2). For the MRPs with marginal differences in their molecular masses, particularly the low molecular mass MRPs (Fig. S4*G*), all five models of a given MRP were docked into the cryo-EM densities tentatively assigned to MRPs of similar molecular mass. For example, the assignment of MRP S26, in which molecular mass does not correlate with volume and surface area, was based on the shape complementarity of the MRP fold and the cryo-EM density (Fig. S5). Using this approach, we were able to assign cryo-EM mass for 12 of 16 MRPs (Fig. 1 *C* and *D*). Each docked model was subjected to 100-ps MDFF-based simulations. All 12 docked models retained their fold during the simulation process, further supporting a complementarity between the MRP fold and the assigned cryo-EM mass. An independent assignment of density for MRP S29 using this method also matched the immuno-EM localization of this MRP on the mito-SSU (16) and gave us further confidence in assigning positions for the rest of the mito-specific MRPs. For the remaining four MRPs (S22, S36, S38, and S39) that could not be docked into assigned cryo-EM segments the predicted I-TASSER folds may be inaccurate. The assignment of these four MRPs in our map is based primarily on earlier biochemical studies (see ref. 17 and/or correlation between molecular mass of the MRP and volume and surface area of the cryo-EM mass in Fig. S4*G*).

Modeling of the Mito-Large Subunit. We have modeled the mito-large subunit (LSU) by docking components of our previously reported LSU model (PDB ID code: 2FTC) (18) and the coordinates of the mito-specific MRPs and unidentified α-helices and double-helical rRNA segments from the recently reported LSU model (PDB ID code 4CE4) (19) into the LSU portion of the 55S cryo-EM map. Both these models are in excellent agreement with each other and with our current cryo-EM map. The I-TASSER homology models of some of the homologous mito-LSU MRPs (e.g., MRP L1, which was absent in either of the previously reported models) also were docked into the cryo-EM map. The clashes, mostly among the side-chain atoms of the docked models, were removed using Coot (11). The combined 55S model was energy minimized and subjected to MDFF for 50 ps. The bridges were identified based on a distance of less than 4 Å between the nearest components of the two subunits and were further confirmed by analyzing cryo-EM densities at the subunit interface of the 55S map.

1. Sharma MR, et al. (2003) Structure of the mammalian mitochondrial ribosome reveals an expanded functional role for its component proteins. *Cell* 115(1):97–108.
2. Cannone JJ, et al. (2002) The comparative RNA web (CRW) site: An online database of comparative sequence and structure information for ribosomal, intron, and other RNAs. *BMC Bioinformatics* 3:2.
3. Wimberly BT, et al. (2000) Structure of the 30S ribosomal subunit. *Nature* 407(6802): 327–339.
4. Tung CS, Joseph S, Sanbonmatsu KY (2002) All-atom homology model of the *Escherichia coli* 30S ribosomal subunit. *Nat Struct Biol* 9(10):750–755.
5. Weiner SJ, et al. (1984) A new force field for molecular mechanical simulation of nucleic acids and proteins. *J Am Chem Soc* 106(3):765–784.
6. Zuker M (2003) Mfold web server for nucleic acid folding and hybridization prediction. *Nucleic Acids Res* 31(13):3406–3415.
7. Tung CS (1997) A computational approach to modeling nucleic acid hairpin structures. *Biophys J* 72(2 Pt 1):876–885.
8. Roy A, Kucukural A, Zhang Y (2010) I-TASSER: a unified platform for automated protein structure and function prediction. *Nat Protoc* 5(4):725–738.
9. Wriggers W (2010) Using Situs for the integration of multi-resolution structures. *Biophys Rev* 2(1):21–27.
10. Pettersen EF, et al. (2004) UCSF Chimera—a visualization system for exploratory research and analysis. *J Comput Chem* 25(13):1605–1612.
11. Emsley P, Lohkamp B, Scott WG, Cowtan K (2010) Features and development of Coot. *Acta Crystallogr D Biol Crystallogr* 66(Pt 4):486–501.
12. Trabuco LG, Villa E, Schreiner E, Harrison CB, Schulten K (2009) Molecular dynamics flexible fitting: A practical guide to combine cryo-electron microscopy and X-ray crystallography. *Methods* 49(2):174–180.
13. Chen VB, et al. (2010) MolProbity: All-atom structure validation for macromolecular crystallography. *Acta Crystallogr D Biol Crystallogr* 66(Pt 1):12–21.
14. Pintilie GD, Zhang J, Goddard TD, Chiu W, Gossard DC (2010) Quantitative analysis of cryo-EM density map segmentation by watershed and scale-space filtering, and fitting of structures by alignment to regions. *J Struct Biol* 170(3):427–438.
15. Haque ME, Koc H, Cimen H, Koc EC, Spremulli LL (2011) Contacts between mammalian mitochondrial translational initiation factor 3 and ribosomal proteins in the small subunit. *Biochim Biophys Acta* 1814(12):1779–1784.
16. Sharma MR, et al. (2011) Three-dimensional localization of the GTP-binding protein within the mammalian mitochondrial ribosome. *Mitochondrion* 11(4):657.
17. Koc EC, et al. (2013) Identification and characterization of CHCHD1, AURKAIP1, and CRIF1 as new members of the mammalian mitochondrial ribosome. *Front Physiol* 4:183.
18. Mears JA, et al. (2006) A structural model for the large subunit of the mammalian mitochondrial ribosome. *J Mol Biol* 358(1):193–212.
19. Greber BJ, et al. (2014) Architecture of the large subunit of the mammalian mitochondrial ribosome. *Nature* 505(7484):515–519.
20. Valle M, et al. (2002) Cryo-EM reveals an active role for aminoacyl-tRNA in the accommodation process. *EMBO J* 21(13):3557–3567.
21. Scheres SH (2012) RELION: Implementation of a Bayesian approach to cryo-EM structure determination. *J Struct Biol* 180(3):519–530.

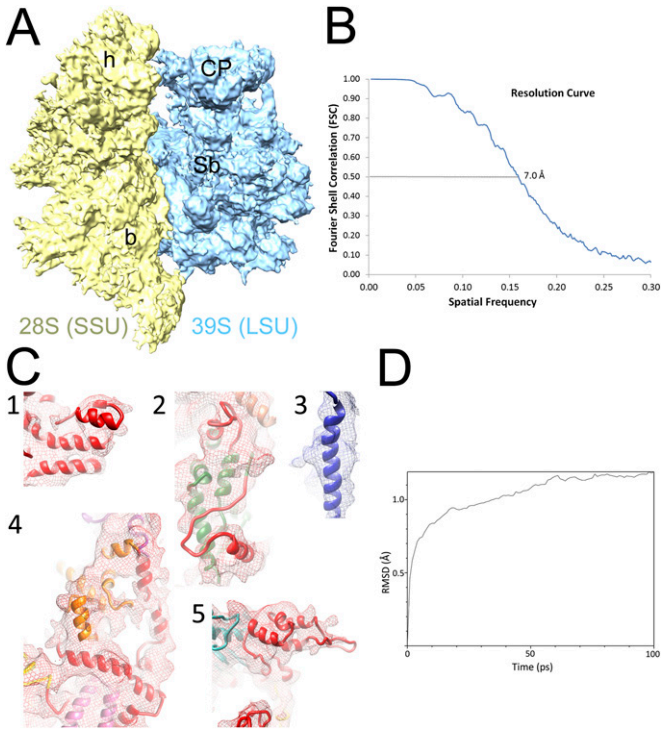

Fig. S1. 3D cryo-EM reconstruction of the 55S mitoribosome and random samples of the modeled densities corresponding to homologous MRPs of the mito-SSU and their mito-specific insertion/extension. (*A*) The segmented cryo-EM map, with SSU (28S, yellow), which is subject of the present study, and the LSU (39S, blue) shown from the shoulder side. Landmarks of the SSU are h, head, and b, body; landmarks of the LSU are CP, central protuberance; and Sb, MRP L11 Stalk base region. (*B*) Resolution curve, with 0.5 cutoff of Fourier Shell Correlation indicated. The segmented SSU portion of the 55S map was used for the molecular interpretation. (*C*) Representative cryo-EM densities (meshwork) for homologous MRPs, with atomic models of their conserved domains (various colors) and mito-specific segments (red): 1, NTE of S9; 2, S7 and its insertion (at the top of the figure) and NTE (at the bottom of the figure); 3, C terminus of S21; 4, CTEs and NTEs of S15; 5, NTE of S5. (*D*) Trajectory of the backbone rmsd with the time (in picoseconds) during MDFF simulation of the 12S rRNA including homologous MRPs.

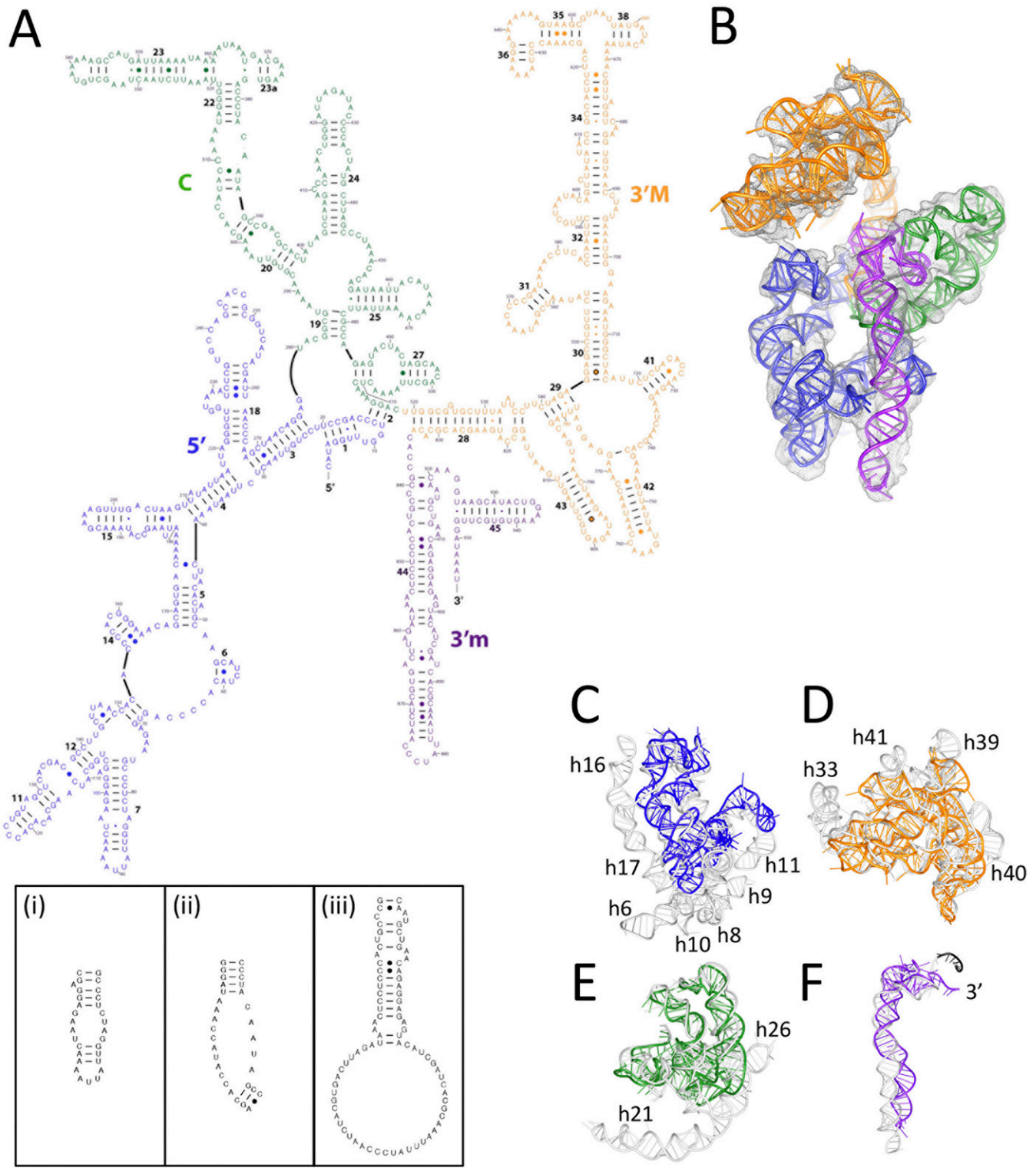

Fig. S2. Secondary and tertiary structures of the 12 S rRNA. (*A*) Secondary structure. Four structural domains of the SSU rRNA are depicted: the 5′ domain (blue, marked by "5′") that forms the body, the central domain (green, marked by "C") that forms the platform, the 3′-major domain (orange, marked by "3′ M") that forms the head, and the 3′-minor domain (magenta, marked by "3′ m") that is part of the SSU body. *Insets* show the secondary structures of three main regions [helices 7 (*i*), 22 (*ii*), and h44 (*iii*)] of the 12S rRNA according to Gutell's prediction (2) that are found to be different in this study. (*B*) Tertiary structure. The 12S rRNA as modeled into the cryo-EM density of the mito-SSU, after applying high-density threshold. (*C*–*F*) 3D folds of the body (*C*), head (*D*), platform (*E*), and h44 (*F*) are shown along with bacterial rRNA folds (gray) to depict deletions of the bacterial rRNA segments (helices numbered with the prefix "h") in the mito-SSU rRNA. In *F*, the anti–Shine–Dalgarno sequence stretch, which is absent in mito-12S rRNA, is depicted in black.

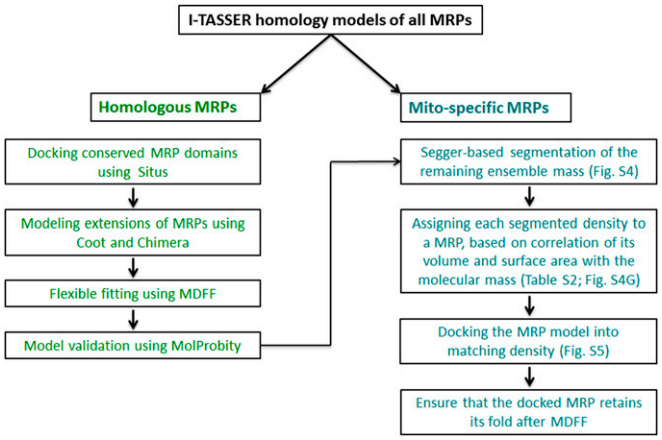

Fig. S3. Flow diagram depicting the steps involved in segmentation and assignment of mito-specific MRPs.

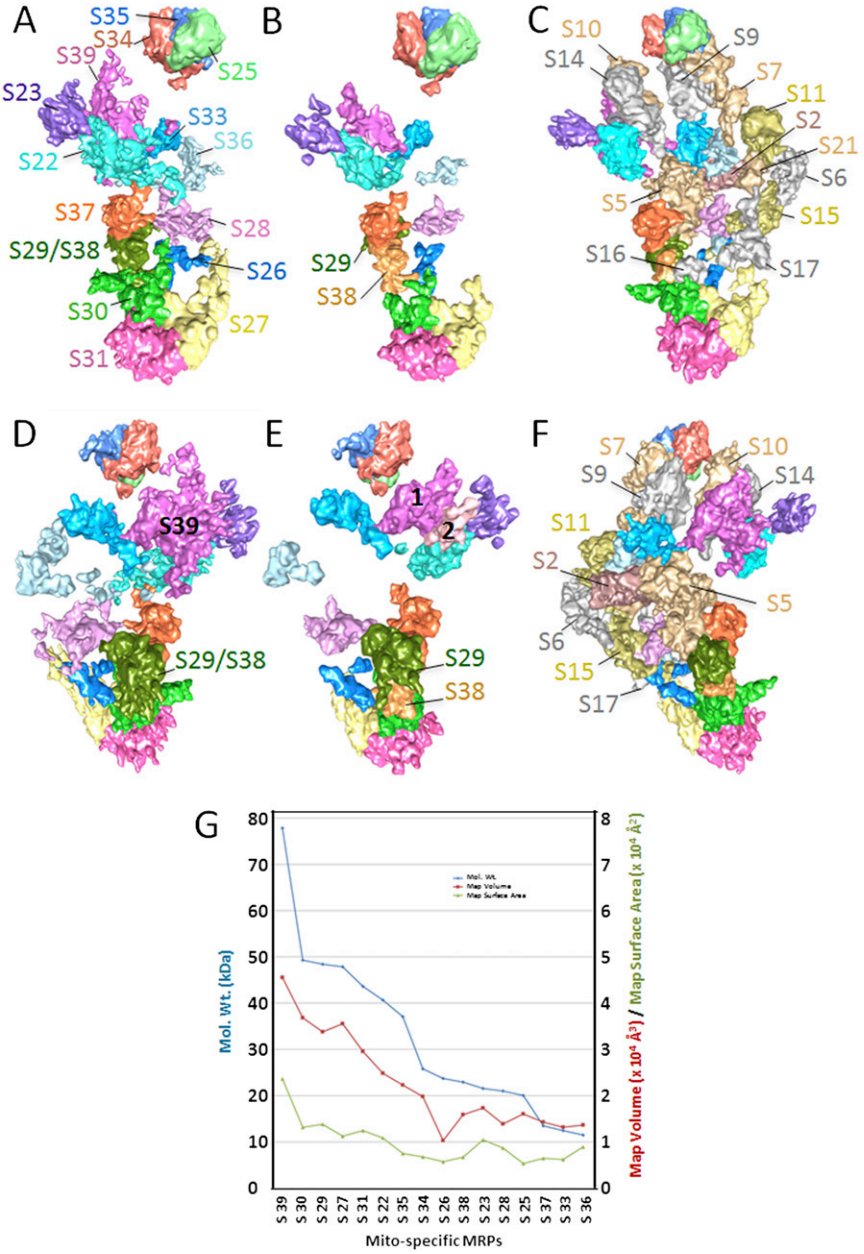

Fig. S4. Segger-based segmentation of the ensemble mass of density corresponding to mito-specific MRPs (i.e., yellow densities shown in Fig. 1 *A* and *B* in the main text). The ensemble density map was segmented into 20, 30, 40, and 50 regions to ascertain consistency in results. We found that the features of the core mass of each segmented density were retained throughout when the number of targeted segments was increased from 20 (*A* and *D*) to 50 (*B* and *E*). However, at a higher number of targeted segments, the size of each segmented density was reduced, primarily because of the further split of peripheral densities within each major segment into additional segments, as expected. For example, each of the large pink and dark green densities (assigned to MRP S39, and S29/38, respectively) in *A* and *D* splits into two masses in *B* and *E*, when segmented into 50 regions. *C* and *F* show the results of segmentation applied on total MRP density, including those corresponding to bacterial homologs, with smoothening step 4. Segmented density for homologous MRP S12 has been removed from *C* and *F* for visual clarity. In *A*–*C*, densities are shown from the side of the SSU interface, whereas in *D*–*F*, they are shown from the solvent side. To enhance visual clarity, smaller segments that could not be assigned to smallest of the MRPs are not shown. (*G*) Correlation between the molecular mass and volume of the segmented densities for mito-specific MRPs (also see Table S2).

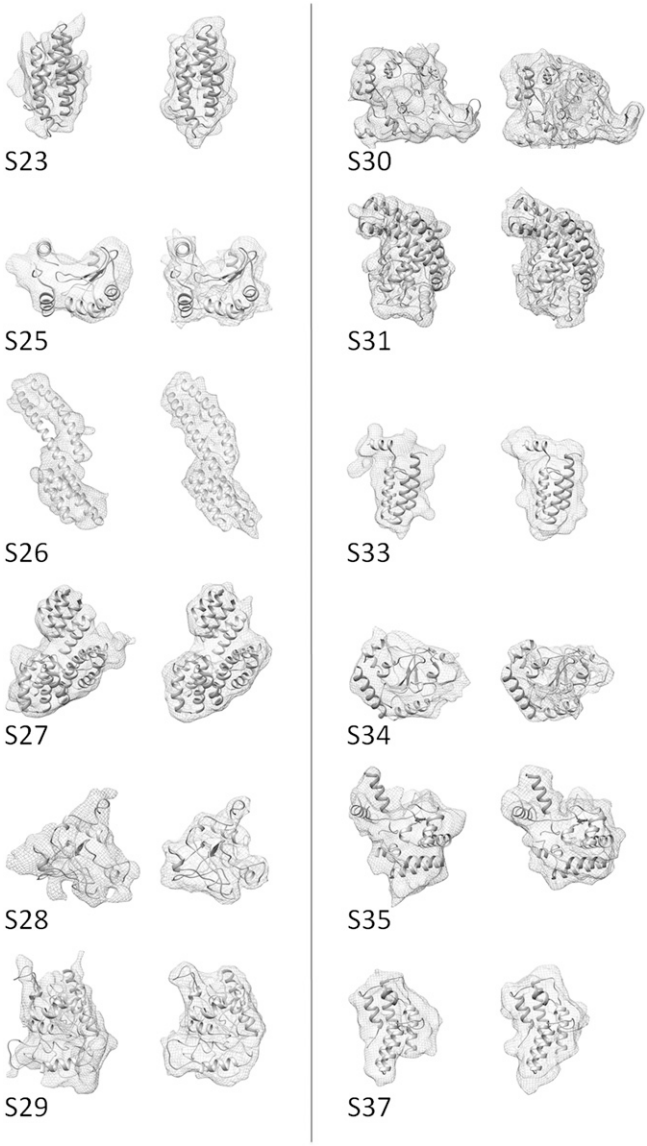

Fig. S5. Dockings of various mito-specific MRPs into corresponding segmented cryo-EM densities. For comparison, in each column MRP models docked into the cryo-EM densities are shown on the left, and low-resolution (~8 Å) simulated densities of the corresponding MRP models are shown on the right. (For CC values of each docked model, see Table S2.)

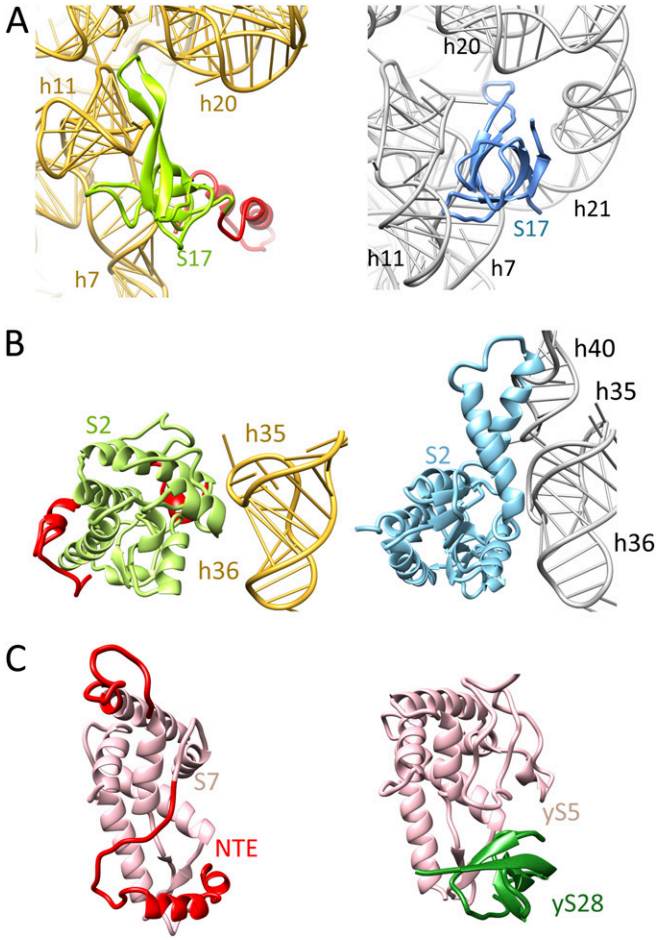

Fig. S6. Effect of deletions of bacterial rRNA helices on the interaction of homologous MRPs S17 (*A*) and S2 (*B*) and the position of the NTE within MRP S7 (*C*). In *A* and *B*, interactions of MRPs are shown on the left, and those of corresponding homologous bacterial proteins are shown on the right. In *C*, the interaction of homologous yeast protein yS5 with yS28, which occupies a position similar to that of the NTE within MRP S7, is shown on the right.

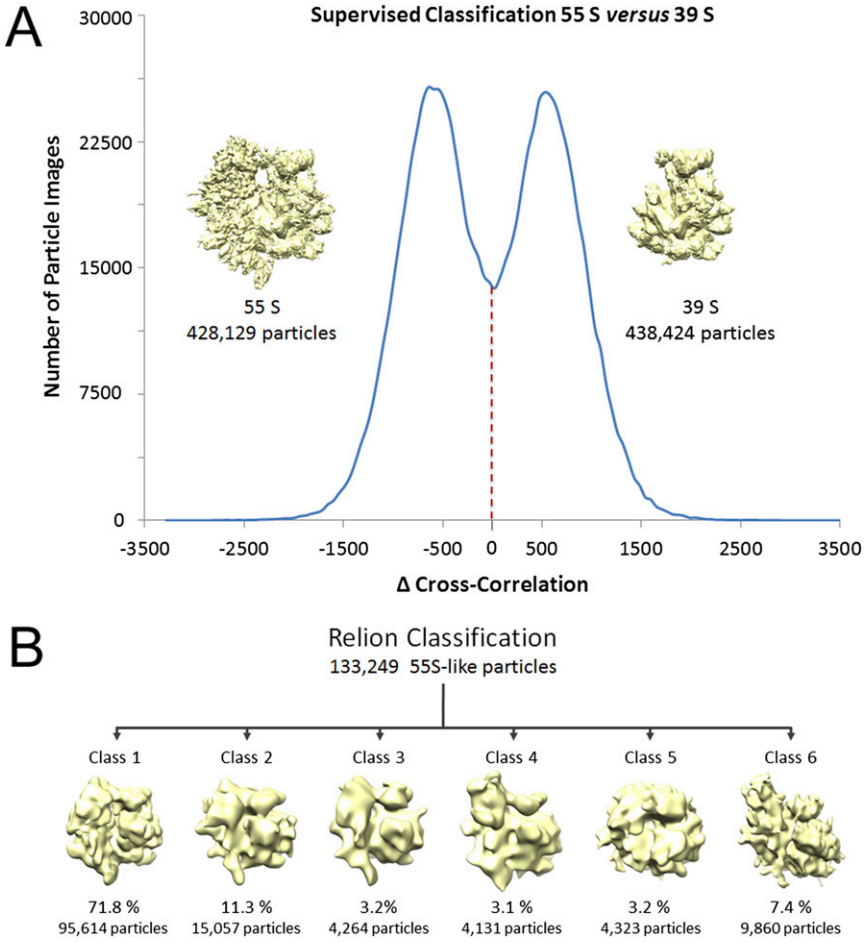

Fig. S7. (*A*) Histogram of supervised classification (20) of particle images obtained for the 55S mitoribosome preparation. Values obtained by computing the difference between the CC coefficients (CCFs) of each experimental projection (image) of the 55S mitoribosome with respect to two reference maps: (*i*) our previously obtained map of the 55S mitoribosome (1), and (*ii*) the map of the computationally isolated 39S portion of the same 55S map. Undecided images, equally dissimilar to the same computationally generated angular projections of either reference, are grouped around 0 on the *x* axis, indicated by a vertical red line. Differences in CCF values are expressed in arbitrary units. The number of images corresponding to each projection of the reference map is shown on the *y* axis. (*B*) Relion-based classification (21) of a small portion of the images classified as 55S particles from the supervised classification step into six classes. This classification yielded a major class in which ∼70% of the particle images closely resembled the 55S mitoribosome structure. The remaining ∼30% of the particle images were distributed among five different small classes with varying degrees of conformational and compositional heterogeneity. This classification also indicated that the central protuberance region of the mito-LSU is highly divergent. We used this statistical information to remove ∼30% of the images with lowest CCF values from the total images that classified with the 55S reference.

Table S1. Homologous MRPs and their mito-specific insertions and/or extensions

Serial no.	MRP	No. of amino acids	MTS	Mito-specific segments	Identity/similarly*	Accession no.**
1	S2	293	1–49	50–75, 277–293	30/43	P82923
2	S5	430	1–88	89–209, 377–430	27/42	Q2KID9
3	S6	124	—	—	26/32	P82931
4	S7	242	1–38	39–81, 121–141	34/56	Q3T040
5	S9	396	1–67	68–267	40/53	Q58DQ5
6	S10	201	—	1–75, 175–201	32/51	P82670
7	S11	197	1–24	25–68,	43/59	FIN498
8	S12	139	1–30	—	52/63	Q29RU1
9	S14	128	—	1–27	37/55	Q6B860
10	S15	256	1–53	54–94, 188–256	28/56	E1BBB4
11	S16	135	1–15	97–135	45/68	P82915
12	S17	130	—	90–130	29/51	E1BF33
13a	S18A	196	1–38	39–60, 137–196	40/58	F1MJC2
13b	S18B	258	1–21	22–95, 170–258	28/54	F1N059
13c	S18C	143	1–39	40–51, 126–143	55/71	P82917
14	S21	87	—	1–30, 80–87	32/51	P82920
15	S24†	167	1–43	—	—	Q2M2T7

MTS, putative mitochondrial targeting sequences.
*Sequence identity/similarity with homologs in *Escherichia coli* 30S ribosome.
†MRP S24 has no bacterial sequence homolog but is a structural ortholog of the NTD of bacterial S3.
**Gene Bank and Swiss Prot.

Table S2. Parameters considered in assignment of the segmented mito-specific MRP densities

Serial no.	MRP	Molecular mass	Volume, Å^3	Area, Å^2	No. of amino acids	MTS (putative)	Region docked	CC
1	S22	40,653	24,810	10,900	359	1–32	Nd	N/A
2	S23	21,564	17,340	10,480	190	—	49–190	0.85
3	S25	20,042	16,070	5,321	173	—	9–131	0.83
4	S26	23,759	10,350	5,751	205	1–43	44–83 92–183	0.74
5	S27	47,891	35,590	11,280	415	—	140–415	0.87
6	S28	21,028	13,900	8,716	189	1–29	55–182	0.82
7	S29	48,413	33,760	13,820	397	—	65–397	0.78
8	S30	49,325	36,800	13,200	435	1–14	15–96 133–309 331–435	0.76
9	S31	43,648	29,570	12,450	386	1–59	67–137 177–257 292–386	0.77
10	S33	12,445	13,150	6,227	106	—	1–106	0.87
11	S34	25,843	19,840	6,817	218	1–19	30–204	0.87
12	S35	37,046	22,300	7,542	325	1–36	62–229 250–325	0.79
13	S36	11,546	13,680	8,991	103	—	Nd	N/A
14	S37 (CHCHD1)	13,546	14,320	6,465	118	—	1–114	0.85
15	S38 (AURKAIP1)	22,906	15,890	6,752	199	1–13	Nd	N/A
16	S39 (PTCD3)	77,781	45,510	23,630	688	1–38	Nd	N/A

CC, cross-correlation between the docked model and corresponding cryo-EM density; CHCHD1, coiled-coil-helix-coiled-coil-helix domain containing protein1. We observed consistency in correlation between a cryo-EM density volume and molecular mass with docking results for the higher molecular mass (>25 kDa) MRPs, with the exceptions of S27 and S29 (Fig. S4*E*). For the lower molecular mass (<25–10.5 KDa) MRPs, where differences in molecular mass were insignificant, docking results (Fig. S5) were used as a guide for the final assignment. N/A, not applicable. Nd, not determined.

Table S3. Distribution of MRPs in three structural domains of the mito-SSU

SSU	MRPs
Body	S5, S12, S16, S17, S26, S27, S28, S29 (DAP3), S30, S31, S37(CHCHD1), and [S38]
Platform	S6, S11, S15*, S18, and S21
Head	S2, S7, S9, S10, S14, [S22], S23, S24†, S25, S33, S34, S35, [S36], and [S39(PTCD3)]

Bracketed MRPs were not modeled. DAP3, death-associated protein 3.
*Because of its tight interactions with MRP S17, MRP S15 is described in *SSU Body* in the main text.
†S24 is a structural ortholog of the N-terminal domain of bacterial S3.

Table S4. Composition of intersubunit bridges in the 55S mitoribosome

		28S (SSU)		39S (LSU)	
Bridge	Type	12S rRNA or MRP	Nucleotide/amino acid position	16S rRNA or MRP	Nucleotide/amino acid position
B1a	Protein–protein	S25*	Ns	U-L	—
B1b	Protein–protein	S25*	Ns	U-L	—
B1c	Protein–protein	S25	Ns	U-L	—
B1d	Protein–protein	S25	Ns	U-L	—
B2a	RNA–RNA	h44	844, 914	H69	919
B2b	RNA–RNA	h24	424–425	H69	927–928
		h45	934–937	H69	925–929
B2c	RNA–RNA	h24	417–418	H67	890–891
		h24	404	H67	887
B2d	RNA–RNA	H27	498	H67	886
B2e	RNA–RNA	h24	407	H66	857
B3	RNA–RNA	h44	855–858, 902–904	H71	954–956, 964–967
B5	RNA–protein	h44	860–861	L14	45–46
B7a	RNA–RNA	h23	345–347	H68	901–903
B7c	Protein–protein	S6	80, 84	L2	174, 178
B9	Protein–protein	S27	Ns	U-L	—

Prefixes "h" and "H": (columns 3 and 5) refer to 12S- and 16S-rRNA helices, respectively. Prefixes "S" and "L" (columns 3 and 5) refer to MRPs of the SSU and LSU, respectively. Ns, not specified; U-L, unassigned MRP(s) of the LSU.
*Most likely correspond to unmodeled C-terminal segment of the mito-specific MRP S25. However, the density corresponding to these two bridges is not resolved in our map and segments readily with the mito-LSU.